RSC Advances

ROYAL SOCIETY OF CHEMISTRY

www.rsc.org/advances

Journal Name

ARTICLE

Electrodeposition of polyaniline on three-dimentional Graphene hydrogel as a binder-free supercapacitor electrode with high power and energy densities†

Received 00th January 20xx,
Accepted 00th January 20xx

DOI: 10.1039/x0xx00000x

www.rsc.org/

Shuya Gao, Li Zhang,* Yadong Qiao, Pei Dong, Jun Shi and Shaokui Cao*

Construction of a 3D graphene-based hybrid electrode with an optimized porous structure remains an attractive topic. Herein, we used the highly conductive graphene hydrogel (GH) with a well-defined 3D macroporous structure as a support to electrodeposite polyaniline (PANI), aimed to improve the energy density of GH-based capacitor electrode without deteriorating its high power capability. The as-prepared GH/PANI heterostructure with thin PANI layer conformally coated on the GH framework totally retains the native hydrogel pore structure and its high surface area, which facilitates the effective electron and ion transport within the electrode and thus endows GH/PANI composite electrode with excellent electrochemical properties such as a specific capacitance of 710 F g^{-1} at 2 A g^{-1} and 73% capacitance retention upon a current increase to 100 A g^{-1}. Moreover, the assembled symmetric supercapacitor device based on GH/PANI heterostructure electrode delivers a maximum energy density and power density of 24 Wh kg^{-1} and 30 kW kg^{-1}, respectively, and also exhibits a good cycling stability with 86% capacitance retention after 1000 cycles. These findings demonstrate the importance and great potential of GH-based heterostructure in the development of high-performance energy-storage systems.

1. Introduction

The growing demand for portable electronics, electric vehicles and load leveling for electric utilities has stimulated intense research on high-performance energy storage devices.[1,2] Supercapacitors, also known as electrochemical capacitors or ultracapacitors, are considered as a promising candidate for energy storage due to high power density, long cycle life, and low maintenance cost.[3,4] However, the energy density of supercapacitors still fall short of the values achieved in lithium ion batteries or fuel cells,[5-7] which restricts the use of supercapacitors from the high and long-term energy application or the use as primary power sources. There are two energy storage mechanisms in supercapacitors: electrical double layer (EDL) capacitance and pseudocapacitance.[8] High specific area carbon, such as active carbon, carbon nanotubes and graphene, has been extensively applied as EDL capacitor electrode materials, which store energy by physical charge accumulation at electrode/electrolyte interface, possessing high power densities and long cycle life but low specific capacitance.[9,10] Contrarily, pseudocapacitor, employing metal oxides or conducting polymers as electrode materials, can delivery high specific capacitance but slow rate capability and poor cycling stability associated with the reversible faradaic transitions of electroactive species of the electrode.[3,11] Thus, much efforts on supercapacitors have been devoted to developing advanced hybrid electrode materials for combining the advantages of the EDL capacitance and pseudocapacitance to achieve both high energy and power densities.[12-14]

So far, most reported hybrid electrode materials based on EDL and pseudocapacitance were prepared in the form of powders.[15-19] These powdery composites not only suffer from phase separation during material preparation, but also need a binder in the subsequent electrode production process to make electrode coatings or tablets, both of which might degrade the electrical and electrochemical properties of the as-prepared electrode, leading to capacitance fading over cycling or at high rates. In view of this, a variety of three-dimensionally (3D) porous carbon monoliths have been devised to integrate with electroactive materials, including carbon nanofoam, template macroporous carbon, hierarchical porous carbon and nanotube/nanofiber assemblies.[20-24] In such configurations, the carbon skeleton acts as both a high surface 3D support for electroactive component and a continuous conduction path for electron, and the through-porous structure provides a channel for electrolyte transport. But the problem associated with these 3D heterostructures is that a large number of meso- and micropores in carbon template are often occluded or cannot be reached by loaded active component, which causes inferior ionic accessibility and thus modest improvement in the electrode performance. In this regard, the design and optimization of 3D carbon-based

School of Materials Science and Engineering, Zhengzhou University, Zhengzhou 450001, China. E-mail: lizhang9@zzu.edu.cn, caoshaokui@zzu.edu.cn.

† Electronic Supplementary Information (ESI) available: Details of experimental section, additional characterizations (Preparation of GH, Raman spectra, SEM and GCD curves). See DOI: 10.1039/x0xx00000x

microstructures (especially the balance between the surface area and pore size distribution) are definitely important since each of the respective material's properties can be dramatically enhanced if an appropriate microstructure is chosen.[12,25]

As a unique carbon nanomaterial, 3D graphene monoliths with a porous network have received increasing attention for the electrochemical energy storage,[26,27] mainly due to their high specific surface areas, ordered macroporous structures, strong mechanical strengths and fast mass and electron transport kinetics.[28] These structural characteristics also enable 3D graphene a promising platform to incorporate with electroactive materials. Recently, some 3D graphene porous films[29-32] and graphene foams,[33-35] which were fabricated with flow-directed and/or template-guided methods, have been used as the support to construct 3D graphene-based composite electrodes, leading to a great increase in specific capacitance and cycling stability. Nevertheless, the oriented structures of 3D graphene porous films formed by flow-directed methods would hinder the rapid electrolyte ions diffusion inside and through the network, and thus lower the utilization of the electrochemical surface area of the electrode especially at high charge-discharge rate. On the other hand, the complicated assembling process and larger pore size of 3D graphene foams by using template-guided approaches could increase the aggregation degree of graphene sheets and compromise its active surface area for loading active component and exerting its EDL energy storage.

In our previous work, the self-assembled graphene hydrogel (GH) with a well-defined 3D macroporous structure was prepared by simple hydrothermal reduction.[36] With an exceptionally high surface area, this mechanically strong and electrically conductive GH has been directly used as binder-free EDL capacitor electrode with excellent energy density (7.6 Wh kg^{-1}) and ultrahigh power density (30 kW kg^{-1}). Herein, we attempted to electrodeposite polyaniline (PANI), a widely used conducting polymer, on the framework of GH, aimed to introduce the unique pseudocapacitive effect of PANI in the GH-based EDL capacitor electrode to improve the energy density without deteriorating its high power capability. As shown in Fig. 1, the resultant GH/PANI heterostructure is composed of a 3D GH conductive framework uniformly coated with PANI thin layer, totally retaining the native GH pore structure and its high surface area, thus guaranteeing the fast and effective charge access and propagation throughout the 3D monolithic architecture. Besides, this heterostructure can enhance the utilization of PANI for pesudocapacitive charge storage and maximize the synergistic effect between GH and PANI. As expected, this conformal composite exhibited excellent capacitive behavior with a high specific capacitance of 710 F g^{-1} at a current density of 2 A g^{-1} and a good rate capability up to a current density of 100 A g^{-1}. Moreover, the symmetric supercapacitor device based on GH/PANI heterostructure electrodes presents a maximum energy density and power density of 24 Wh kg^{-1} and 30 kW kg^{-1}, respectively, and a good cycling stability with 86% capacitance retention after 1000 cycles.

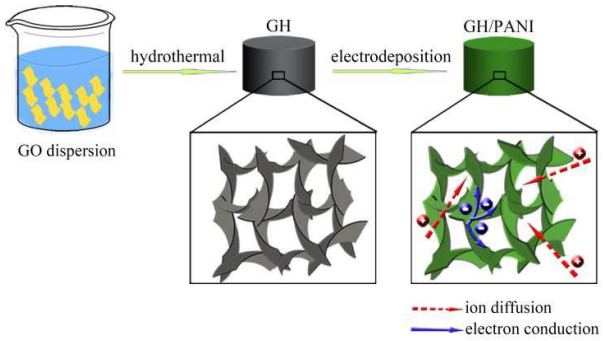

Fig. 1 Schematic illustrating the fabrication process toward GH/PANI composite and 3D ion and electron transport pathway in porous GH/PANI electrode.

2. Experimental section

2.1 Materials

Natural graphite powder (325 mesh) was purchased from Qingdao Huatai Lubricant Sealing S&T Co. Ltd (Qingdao, China). Aniline (Shanghai Chem. Co) was purified through distillation under reduced pressure and stored in a refrigerator before use. All other reagents were of analytical grade and used without further purification.

2.2 Preparation of GH and GH/PANI composites

Graphene oxide (GO) was prepared by oxidation of natural graphite powder (325 mesh) according to a modified Hummers' method as reported previously.[36] In the preparation of GH, a 10 mL portion of 2 mg mL^{-1} homogeneous GO aqueous dispersion was sealed in a 16 mL Teflon-lined autoclave and maintained at 180 ^{o}C for 12h. Then, the autoclave was naturally cooled to room temperature, and the as-prepared GH was taken out with a tweezer and cut into small slices (thickness 1mm) for later use. GH/PANI composites were prepared by electrochemical polymerization of aniline on the framework of GH in a three electrode cell which was constructed with a Pt foil as the counter electrode and Ag/AgCl as the reference electrode. A slice of GH was tied on the other Pt foil by plastic net and used as working electrode. The electrolyte was 1 M H_2SO_4 and 0.05 M aniline. The working electrode was immersed into the electrolyte for several hours to allow the aniline monomer to diffuse into the porous GH. The deposition of PANI was performed at a constant potential of 0.8V *versus* reference electrode for different period (10, 20, 40, and 60 min) on a CHI660D electrochemical analyzer, and the resulting GH/PANI composites were denoted as GP10, GP20, GP40 and GP60, respectively, according to the electrodeposition time. The as-obtained composites were washed repeatedly with deionized water and stored in deionized water.

2.3 Structure Characterizations

Raman spectra were recorded on a RM 2000 Microscopic confocal Raman spectrometer (Renishaw PLC, England) using a 514 nm laser beam. Fourier transform infrared spectra (FTIR) were carried out on a Spectrum GX FTIR system (PerkinElmer). X-ray photoelectron microscopy (XPS) was performed on a ESCALAB 250 photoelectron spectrometer (Thermo Fisher Scientific) with Al Ka (1486.6 eV) as the X-ray source set at 150 W and a pass energy of 30 eV for high resolution scan. Scanning electron micrographs (SEM) were recorded on a Hitachi S-8000 field-emission scanning electron microscopy equipped with an X-ray energy dispersive spectrometer (EDS). Nitrogen adsorption experiments and micropore analysis were conducted at 77 K using a TriStar II 3020 (Micromeritics Instrument Corporation) apparatus. Before adsorption measurements, the samples were degassed in vacuum at 473 K for 12 h. The specific surface areas of the freeze dried hydrogels were calculated by Brunauer-Emmett-Teller (BET) analyses of their adsorption isotherms. Elemental analysis was conducted on a CE440 elemental analyzer. Atomic force microscopy (AFM) image of GO sheets deposited on a freshly cleaved mica surface was taken out by using a Nanoscope III MultiMode SPM (Digital Instruments) with an AS-12 ("E") scanner operated in tapping mode in conjunction with a V-shaped tapping tip.

2.4 Electrochemical Measurements

Electrochemical experiments were performed using a CHI660D potentiostat (CH instrument inc.) with a three-electrode system for the obtained GH and GH/PANI composites and a symmetrical two-electrode configuration for assembled supercapacitor devices. In a three-electrode system, electrochemical characterization by cyclic voltammetry (CV) and galvanostatic charge/discharge (GCD) measurements were performed in 1 M H_2SO_4 with the same equipment as used for the preparation of GH/PANI composites by electrochemical deposition (section 2.2). The mass specific capacitances (C_s) were calculated by using the equations $C_s = I\Delta t/(m\Delta V)$, where I is the constant discharge current, Δt is the discharging time, m is the mass of single electrode, ΔV is the voltage drop upon discharging (excluding the IR drop). For a two-electrode system, two slices of active material (thickness 1mm)were separated by a filtrate paper soaked with electrolyte (1 M H_2SO_4) and used as the supercapacitor electrode materials. Two Pt foils were used as the current collectors. All the components were assembled into a layered structure and sandwiched between two PTFE sheets.The electrochemical performance of the supercapacitor cells were evaluated by GCD with potential range of 0 to 1 V and electrochemical impedance spectroscopy (EIS) in the frequency range of 10^5-0.01 Hz at a 10 mV amplitude referring to open circuit potential. Energy density (E) and power density (P) for the supercapacitor cell in the Ragone plot were calculated from GCD results by using the equations $E= 0.5C\Delta V^2/M$ and $P = E/\Delta t$, respectively, where C is the measured capacitance of supercapacitors, M is the total mass of two electrode materials, ΔV is the operating potential window, and Δt is the discharging time.

3. Results and discussion

Graphene hydrogel (GH) can be easily prepared by one-step hydrothermal reduction of GO aqueous dispersion (Fig. S1). The obtained GH is conductive and highly accessible for electrolyte and aniline molecules, thus can be used as porous electrode to deposit PANI using the electrochemical method. Compared with *in situ* chemical deposition,[29,30,34,37] the electrochemical method can have better control over the deposition process, and ensure that the nucleation and growth of PANI occur on the surface of graphene sheets rather than in the solution. The nucleation of PANI in the solution is unwanted here because it may cause nonuniformity of the

Table 1 Weight contents of PANI in composites, BET specific surface areas (S_A), specific capacitances (C_s) at different current densities, and capacitance retentions (C_r) for various electrode materials.

Sample	PANI (wt%)	S_A ($m^2\ g^{-1}$)	C_s ($F\ g^{-1}$) at 2 A g^{-1}	C_s ($F\ g^{-1}$) at 100 A g^{-1}	C_r (%)
GH	0	305	230	177	77
GP10	18	258	342	261	76
GP20	29	236	710	517	73
GP40	42	162	472	336	71
GP60	50	105	364	225	61

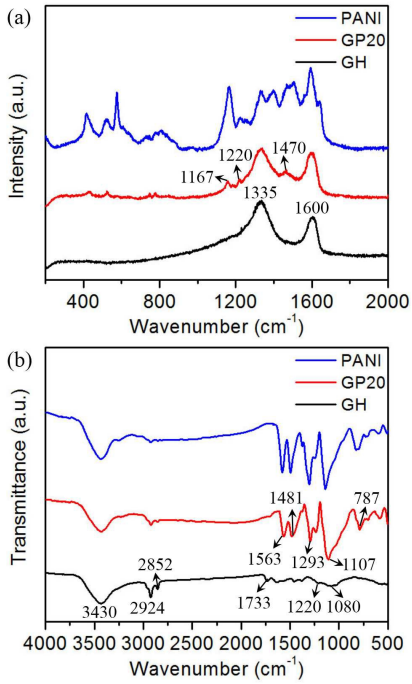

Fig. 2 Raman (a) and FTIR (b) spectra of GH, GP20 and PANI samples.

final product. The successful deposition of PANI on the skeleton of porous GH was confirmed by the Raman and FTIR spectra (Fig. 2). As shown in Fig. 2a, only two bands at 1335 and 1600 cm^{-1} are found in the Raman spectrum of GH, which can be attributed to the well-documented D and G bands of reduced GO.[38] After the electrodeposition of PANI, some new bands arising from doped PANI can be indexed at 1167, 1220 and 1470 cm^{-1} for the composite, which correspond to C-H bending in the benzenoid groups, C-N stretching of the polaronic units and C=N stretching of the quinonoid units in PANI, respectively.[35] It can be seen that the intensities of Raman bands associated with PANI were increased with the increase of deposition time (Fig. S2), indicating that more and more PANI was electrodeposited on the graphene surfaces in GH and thus the loading amount of PANI can be simply controlled by deposition time. The weight contents of PANI in composites with different electrodeposition time were determined by element analysis and listed in Table 1. From Fig. 2b, the FTIR spectrum of GH displays obvious bands at 3430, 2924 and 2852 cm^{-1}, corresponding to –OH, -CH and $–(CH)_n$ vibrations respectively, and some subdued bands owing to oxygen-containing groups at 1733 (C=O), 1220 (C-O-C), and 1080 cm^{-1} (C-O). These results are attributed to the presence of partially reduced GO.[24] In comparison, the FTIR spectrum of the composite (take GP20 for example) shows some new bands attributed to PANI, including C=C stretching of quinonoid and benzenoid rings at 1563 and 1481 cm^{-1} respectively, C-N stretching of secondary aromatic amines at 1293 cm^{-1}, C-H in-plane bending of quinonoid ring at 1107 cm^{-1}, and C-H out-of-plane bending for the aromatic ring at 787 cm^{-1}.[39] The presence of these bands suggests the successful coating of PANI on the skeleton of GH. Additionally, compared with pure PANI, the intensified “electronic-like band” at 1107 cm^{-1} and the red-shift of PANI characteristic peaks in the spectrum of composite may result from the strong interaction between PANI and graphene sheets.[40]

The surface chemical compositions and valence states of GH/PANI composite were characterized by XPS. As shown in Fig. 3a, the survey XPS spectrum of GP20 exhibits distinct peaks of S 2p, C 1s, N 1s and O 1s, suggesting the presence of graphene and PANI in the composite sample. The existence of sulfur element here is attributed to the polymerization of aniline monomers under the condition of adding sulfuric acid. The C 1s core-level spectrum of GP20 (Fig. 3b) is deconvoluted into five subpeaks, which are related to C=C/C-C (284.7 eV), C-N/C=N (285.8 eV), C-O (286.6 eV), C=O (287.8 eV), O-C=O (289.3 eV). These peaks correspond to the different carbon bond structures in PANI as well as GH. Moreover, the deconvolution of N 1s core-level spectrum (Fig. 3c) results in three peaks ascribed to PANI: quinoid imine (-N=) at 398.5eV, benzenoid amine (-NH-) at 399.3 eV, and nitrogen cationic radical (N^+) at 401.3 eV. The last peak is indicative of the doped state of PANI in the composite. Based on the quantitative analysis of the deconvoluted N 1s spectrum, a N^+/N ratio of 0.26 was obtained, revealing a high proton doping level for the deposited PANI on GH. A high doping level affords a better electronic conductivity, which would lead to an enhanced pseudocapacitive performance.[23,41]

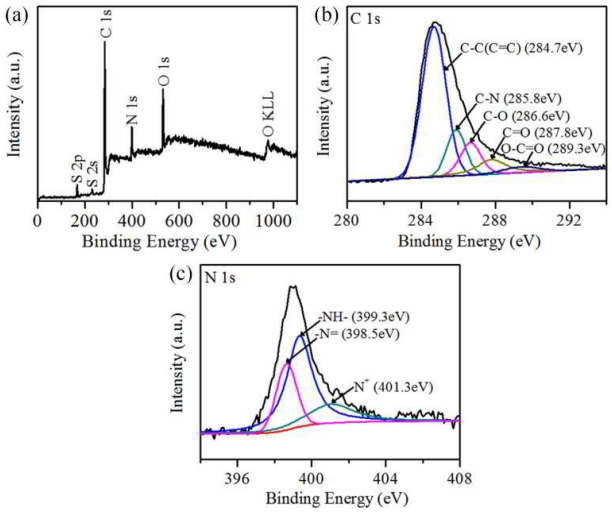

Fig. 3 (a) XPS survey spectrum, (b) C 1s core-level spectrum, and (c) N 1s core-level spectrum of GP20 composite.

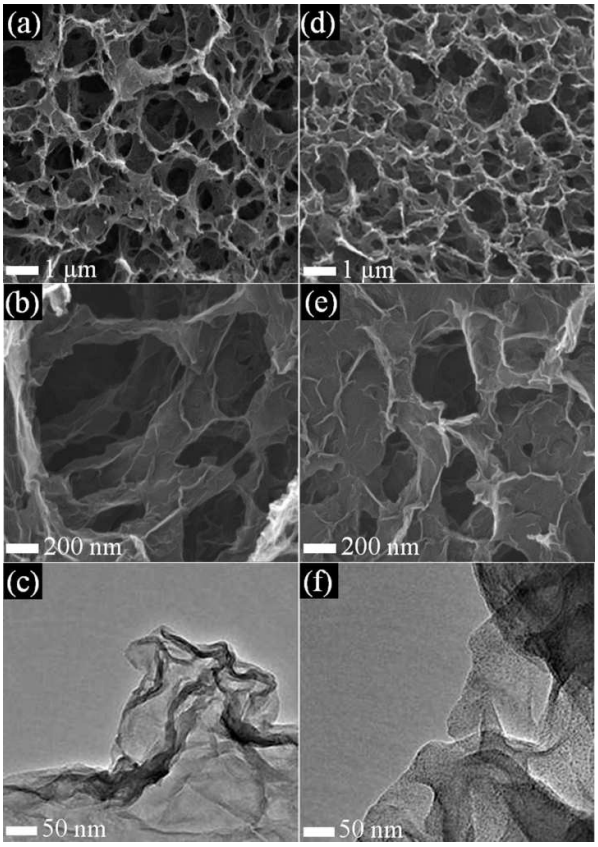

Fig. 4 SEM and TEM images of GH (a-c) and GP20 (d-f). Low-magnification SEM images (a, d) showing the 3D macroporous structure. High-magnification SEM images (b, e) and low-magnification TEM images (c, f) showing the morphology of graphene and graphene/PANI sheets.

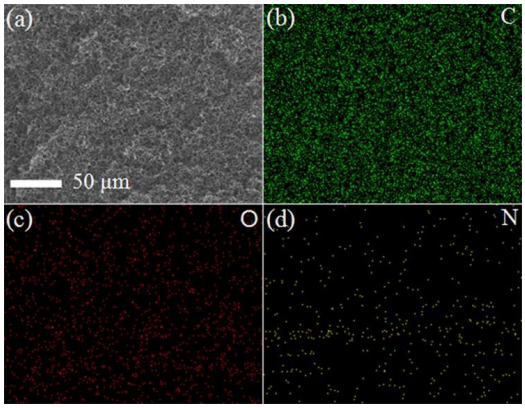

Fig. 5 Large-area cross-section SEM image of GP20 (a) and corresponding EDS element mapping images of C (b), O (c) and N (d) in the same area.

The morphologies of lyophilized GH and GH/PANI composites were observed by SEM and TEM. From Fig. 4a and b, the bare GH possesses a fully interconnected porous network which was formed by physical cross-linking of graphene sheets in 3D space via π-π stacking interactions. The pore sizes of GH range from submicrometer to several micrometers, offering a good compromise between infiltration rate and surface area for depositing active materials. The resulting GP20 composite inherits the 3D porous structure of GH (Fig. 4d) and the graphene/PANI sheets in GP20 exhibit a similar morphology to the pristine graphene sheets in GH (Fig.4e), implying the deposited PANI layer is extremely thin. The thin layer of PANI on the graphene sheets can be identified by careful examination of the TEM image in Fig. 4f, which indicates the uniform layer of fine PANI particles is decorated on the surface of graphene sheet, forming a conformal structure. This skin-like surface plating is similar to the formation of PANI thin layer on a graphene scaffold[42,43] or in a macroporous carbon[23] by electropolymerization of aniline. It is also seen from Fig. S3 that the thickness of graphene/PANI sheets in composites gradually increases with deposition time. When the electrodeposition time was less than 40 min, the native porous structure of GH in composites could be well-maintained, which is significant for the diffusion of electrolyte into the GH/PANI heterostructure. Furthermore, the large-area cross-section SEM and corresponding EDS element mapping (Fig. 5) show a homogenerous distribution of PANI throughout the internal volume of the heterostructure, which can be attributed to the well-defined macroporous structure of GH that allows aniline molecules to gain access onto the graphene surface even deep inside the monolith during the PANI deposition.

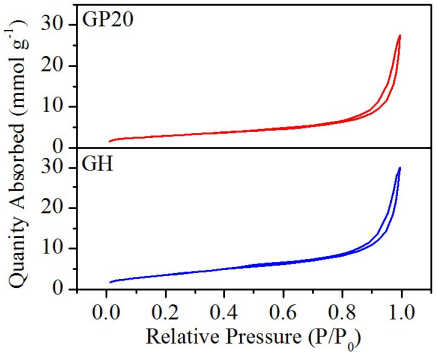

Fig. 6 N_2 adsorption-desorption isotherms of lyophilized GH and GP20 samples.

The changes of pore structure and surface area as a result of PANI incorporation were tracked by N_2 sorption measurements. Fig. 6 shows the N_2 adsorption-desorption isotherms of lyophilized GH and GP20, and both the curves are characterized by type II isotherms with no hysteresis loops, reflecting that no micropores or mesopores exist in these hydrogels. With the deposition of PANI, the measured Brunauer-Emmett-Teller (BET) specific surface areas of GH decreased from 305 $m^2 g^{-1}$ (normalized to the mass of GH) to 236 $m^2 g^{-1}$ (normalized to the total mass of GH skeleton and loaded PANI) for GP20. Given that the conformal structure was formed between the featureless PANI thin film and graphene sheets in GP20, the specific surface area of the composite can be recalculated to be 332 $m^2 g^{-1}$ (normalized to the mass fraction of GH skeleton, which is 0.71 in GP20 composite), implying the PANI loading indeed slightly increased the exposed surface area of GH. The large surface area of GH/PANI composite can ensure the full utilization of electrochemical properties of both graphene and PANI. The other lyophilized composite hydrogels exhibit similar N_2 sorption isotherm characteristics (not shown), and their corresponding BET specific surface areas (S_A) are listed in Table 1. It can be seen that the S_A of the composites decreases with increasing the content of PANI, which would be due to the increased

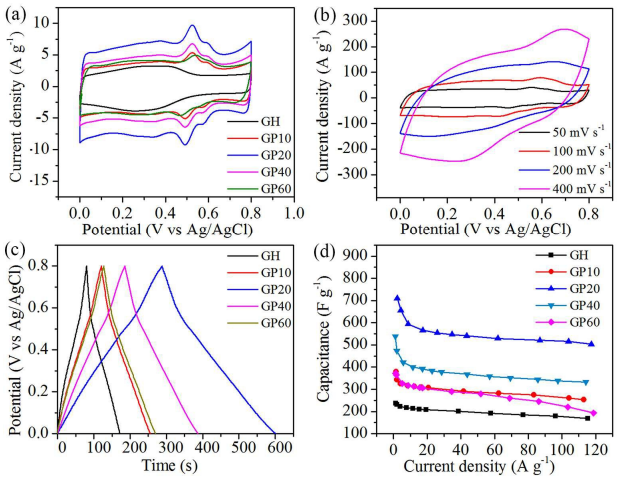

Fig. 7 (a) CV comparison of GH electrode with GH/PANI composites at the scan rate of 10 mV s^{-1}; (b) CV curves at different scan rates for GP20; (c) GCD curves of GH electrode and GH/PANI composites at a current density of 2 A g^{-1}; (d) Plots of specific capacitance versus discharging current density for GH/PANI composites compared with GH electrode.

thickness and mass of deposited PANI in the composites.

The elctrochemical capacitive properties of GH/PANI composites were firstly investigated by cyclic voltammetry (CV) and galvanostatic charge/discharge (GCD) tests using a three-electrode system in 1M H_2SO_4 aqueous solution. Fig. 7a compares the CV curve of GH with its composite electrodes at the scan rate of 10 mV s^{-1}. The CV curve of GH shows a nearly rectangular shape which is characteristic of the EDL capacitance of carbon-based materials.[43] A couple of inconspicuous redox waves at about 0.3V are assiciated with the residual oxygenated groups on the reduced GO sheets. However, all the composites display the enlarged CV curve loops which contain a quasi-rectangular shaped baseline current and two pairs of redox waves in the potential range of 0.2 to 0.6 V. The baseline current is attributed to the EDL capacitance of the electrode and the redox peaks are associated with the leucoemeraldine/emeraldine and emeraldine/pernigraniline transition of PANI,[44] revealing that the capacitive response comes from the combination of EDL capacitive behaviour of GH and the faradaic capacitance of deposited PANI layer. Among all the composite electrodes, GP20 possesses the largest area of surrounded CV loops, demonstrating an optimized electrochemical performance. Moreover, the detailed CV behaviors of GP20 at different scan rates are displayed in Fig. 7b. With the scan rate increasing from 50 to 400 mV s^{-1}, the CV loop area rises successively with slight changes in the CV shape, and a rapid current response upon voltage reversal occurs at all the scan rates, revealing the good charge propagation behavior and rapid ion reponse of GP20 electrode.[12,29]

Fig. 7c shows the GCD curves of GH electrode and GH/PANI composites at a current density of 2 A g^{-1}. All curves are in almost symmetric triangular shape, indicative of the reversible behavior of the ideal capacitor. Compared with GH electrode, the GH/PANI composites show slight curvatures in their GCD curves and much longer discharging durations, due to the presence of large pseudocapacitances of PANI. Meanwhile, much small IR drops are found in all these curves, suggesting good electric conductance of the electrode and efficient use of a capacitance current.[45] The specific capacitances (C_s) of GH and GH/PANI composites were calculated from the slope of discharge curves and the results are listed in Table 1. At the current density of 2 A g^{-1}, a maximum C_s of 710 F g^{-1} is obtained with GP20, three times that of the bare GH electrode (230 F g^{-1}), indicating that C_s of composite hydrogel was remarkably improved due to the pseudocapacitance contributed by PANI. It is worth noting that the C_s of GP20 exceeds or weighs against those of reported 3D graphene/PANI composite electrodes, such as oriented 3D graphene /PANI composite films (530 F g^{-1} at 10 A g^{-1} [29] and 385 F g^{-1} at 0.5 A g^{-1} [30]), electrochemically reduced 3D graphene/PANI composite (560 F g^{-1} at 1.4 A g^{-1} [32]), and Ni foam templated 3D graphene /nanostructured PANI composites (751 F g^{-1} at 1 A g^{-1} [33] and 790 F g^{-1} at 1 A g^{-1} [34]). This large specific capacitance of GH/PANI composite electrode can be attributed to the synergistic effect between GH support and deposited PANI thin layer. The highly conductive GH scaffold provides a large surface area for forming a high EDL capacitance as well as for conveniently depositing PANI. The formed GH/PANI heterostructure with thin PANI layer conformally coated on the GH framework totally retains the native hydrogel pore structure, which facilitates the effective electrolyte diffusion and charge transfer at interfaces and ensures full utilization of both the EDL capacitance of GH and the pseudocapacitance contributed by PANI.

It is also found from Table 1 that the C_s values of GH/PANI composites at 2 A g^{-1} do not always increase with the content of PANI. For GP10, the lower C_s (342 F g^{-1}) is due to that the amount of electrodeposited PANI in GP10 is small. However, for the composites with more PANI, such as GP40 (472 F g^{-1}) and GP60 (364 F g^{-1}), the C_s values decreases with the increase of PANI content. As discussed above, the higher PANI content in composites means thicker coating of PANI. It has been suggested that the faradic reaction mainly occurs at the interface between PANI and the electrolyte due to the electrode kinetic limitations,[46, 47] while the interior portion of PANI in the thick coating is electrochemically inactive and makes no contribution to the charge storage mechanism. This leads to the decrease of C_s in the composites with thick PANI coating. Additionally, the thick PANI layer may block some channels in the porous composite (can be seen from Fig. S3e and infered from the smaller S_A in Table 1), which can hinder the mass transfer and result in lower specific capacitance.

The rate performance of these electrodes was further evaluated by charging/discharging at different current densities (Fig. 7d) and the corresponding results are also listed in Table 1. For GP10, GP20 and GP40 composites, when the current density is increased from 2 to 100 A g^{-1}, more than 70% specific capacitances are maintained. These capacitance retention values are very close to that of GH electrode (77% retention), indicating that the preserved 3D macroporous heterostructure allows for unobstructed electron and ion transport within the composites, thereby generating reversible capacitive behavior even at high charging/discharging rates. However, when thick layer of PANI is deposited (such as GP60), the capacitance retention is decreased to 61%, which is in line with the above conclusion that the excess PANI deposition would block some channels in the porous composite and thus slow down the mass transfer of electrolyte ion.

The capacitive performances of bare GH and optimized GP20 composite were also evaluated in a more practical symmetrical two-electrode supercapacitor system (Fig. 8a). The Ragon plots of GH and GP20 based supercapacitors illustrates the corresponding energy/power densities (Fig. 8b), which were calculated from GCD measurement results based on two-electrode system (Fig. S4). In comparison with GH supercapacitor, the energy densities of GP20 supercapacitor are significantly enhanced, especially in cases with lower power densities. A maximum energy density of 24 Wh kg^{-1} (at power density of 543 W kg^{-1}) was achieved for GP20 supercapacitor, which is more than twice that of GH (8.7 Wh kg^{-1} at power density of 480 W kg^{-1}). The energy density of GP20 supercapacitor drops slowly with the increase of power density, and still retains as 18 Wh kg^{-1} at high power

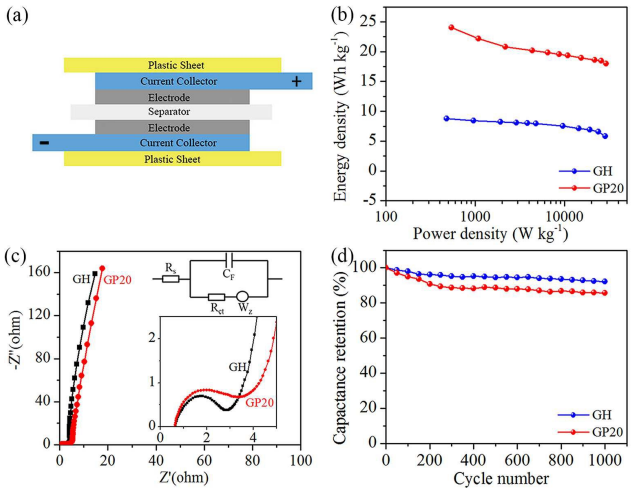

Fig. 8 (a) Schematic diagram of assembled symmetric supercapacitor cells based on GH and GP20; (b) Ragon plots of GH and GP20-based supercapacitors; (c) EIS Nyquist plots of GH and GP20-based supercapacitors in the frequency range of 10^5-0.01 Hz. The insets are the equivalent circuit and the detail with enlarged scale. In the equivalent circuit, R_s represents the internal resistance, R_{ct} is the charge transfer resistance, W_z is the Warburg impedance, and C_F is the electrochemical capacitance; (d) Cycling stability of GH and GP20-based supercapacitors upon charging/discharging at a constant current density of 2 A g^{-1}.

density of 30 kW kg^{-1}. These values are superior to those previously reported symmetric supercapacitors based on graphene/PANI composites,[34,48-51] demonstrating that the unique 3D macroporous heterostructure of GP20 plays an important role in facilitating electron and ion transport and increasing energy storage during the charge storage/deliver processes.

Electrochemical impedance spectroscopy (EIS) measurements were further performed from 0.01 HZ to 1 MHz to analyze the charge-transport kinetics and electrode conducitvity of the assembled suporcapacitors. Fig. 8c presents the EIS Nyquist plots of GH and GP20 based supercapacitors and their corresponding equivalent circuit. Both EIS Nyquist plots exhibit a small semicircle in the high frequency region related to charge transfer resistance (R_{ct}), 45° Warburg section in the middle frequency region (Warburg impedance W_z) associated with the porous structure of the electrode, and a straight line in the low frequency region indicative of capacitive behavior (electrochemical capacitance C_F). At very high frequency, the intercept at X-axis represents a combined internal resistance (R_s) of electrolyte solution resistance, intrinsic resistance of active materials and interfacial contact resistance of active materials and current collectors.[52] This value (0.64 Ω) is almost the same for both GH and GP20, reflecting the incorporation of PANI layer does not impair the electrical conductivity of electrode. The R_{ct} of GP20 (2.44 Ω), obtained from equivalent circuit fitting, is slightly higher than that of GH (2.16 Ω), which is due to the additional faradaic charge transfer resistance at GP20 electrode/ electrolyte interface. However, the 45° Warburg region in the middle frequencies is very short for both GH and GP20, indicating the capability of fast electrolyte diffusion in the macroporous electrode is maintained even after PANI is deposited within the GH matrix.[27]

The cycling performances of GH and GP20-based supercapacitors were tested using a long-term GCD cycling process at a constant current density of 2 A g^{-1}. According to Fig. 8d, GH supercapacitor exhibits an excellent stability over the entire cycle range and keeps 92% of its initial capacitance after 1000 cycles, while GP20 supercapacitor also show a good stability with a capacitance retention of 86% after 1000 cycles. Generally, PANI-based supercapacitors often suffer from a short cycle life due to the swelling and shrinking of the polymer network during the doping-dedoping process. The excellent stability performance of the GP20 supercapacitor is mainly due to that GH provides a flexible, mechanically strong and electrically conductive scaffold to accommodate the volume changes of conformal PANI thin film during charging/discharging process. Besides, the strong adhesion of PANI on graphene sheets through π-π interaction can also maintain the stability. Furthermore, when six different GP20 supercapacitors (which were fabricated independently by the same procedure described in Experimental section) were evaluated, almost the same capacitive performances was obtained, indicating that the fabrication procedures for GP20 sample and its supercapacitor device are reliable and reproducible, which is very important for the practical application of supercapacitor.

4. Conclusions

The GH/PANI composites have been prepared by electrodepositon of a thin layer of PANI on the conductive framework of 3D macroporous GH. The as-prepared GH/PANI heterostructure totally retains the native hydrogel pore structure and its high surface area, which facilitates the effective electron and ion transport within the electrode and thus endows GH/PANI composite electrode with excellent electrochemical properties such as a specific capacitance of 710 F g^{-1} at 2 A g^{-1} and 73% capacitance retention upon a current density increase to 100 A g^{-1}. Moreover, the assembled symmetric supercapacitor device based on GH/PANI heterostructure electrode exhibits a maximum energy density and power density of 24 Wh kg^{-1} and 30 kW kg^{-1}, respectively, and a good cycling stability with 86% capacitance retention after 1000 cycles. These greatly enhanced capacitive performances can be ascribed to choosing GH as a support for PANI, which advantages are summarized as follows: (i) the well-defined and through-connected macroporous structure make it highly accessible to electrolyte ion and molecules; (ii) it provides a large surface area for depositing active materials, thus increasing the utilization of the electroactive regions; (iii) it contributes high EDL capacitance to the overall energy storage; (iv) it serves as a flexible and strong scaffold to relieve the degradation problem during cycling process. All these

characteristics demonstrate that GH can be used as a versatile support for electroactive materials. There is still much room to further improve the electrode performance by tuning the nanostructure and composition of active materials in GH monoliths.

Acknowledgements

This work was financially supported by the National Natural Science Foundation of China (No. 21374106).

References

1 C. Liu, F. Li, L. P. Ma, H. M. Cheng, Adv. Mater., 2010, **22**, E28-E62.
2 N. Armaroli, V. Balzani, Energy Environ. Sci., 2011, **4**, 3193-3222.
3 P. Simon, Y. Gogotsi, Annu. Rev. Nucl. Part., 2008, **S 7**, 845-854.
4 J. R. Miller, Science, 2008, **321**, 650-652.
5 B. Scrosati, Jürgen Garche, J. Power Sources, 2010, **195**, 2419-2430.
6 G. Pagot, F. Bertasi, G. Nawn, E. Negro, G. Carraro, D. Barreca, C. Maccato, S. Polizzi, V. D. Noto, Adv. Funct. Mater., 2015, **25**, 4032-4037.
7 S. Mekhilef, R. Saidur, A. Safari, Renewable and Sustainable Energy Reviews, 2012, **16**, 981-989.
8 P. J. Hall, M. Mirzaeian, S. I. Fletcher, F. B. Sillars, A. J. R. Rennie, G. O. Shitta-Bey, G. Wilson, A. Cruden, R. Carter, Energy Environ. Sci., 2010, **3**, 1238-1251.
9 T. Welton, Chem. Rev., 1999, **99**, 2071-2083.
10 Y. Q. Sun, Q. Wu, G. Q. Shi, Energy Environ. Sci., 2011, **4**, 1113-1132.
11 J. T. Zhang, X. S. Zhao, J. Phys. Chem. C., 2012, **116**, 5420-5426.
12 R. Liu, J. Duay, S. B. Lee, Chem. Commun., 2011, **47**, 1384-1404.
13 S. Bose, T. Kuila, A. K. Mishra, R. Rajasekar, N. H. Kim, J. H. Lee, J. Mater. Chem., 2012, **22**, 767-784.
14 P. Xiong, J. W. Zhu, X. Wang, J. Power Sources, 2015, **294**, 31-50.
15 S. Chen, J.W. Zhu, X.D. Wu, Q.F. Han, X. Wang, ACS Nano, 2010, **4**, 2822-2830.
16 H. L. Wang, H. S. Casalongue, Y. Y. Liang, H. J. Dai, J. AM. Chem. Soc., 2010, **132**, 7472-7476.
17 J. J. Xu, K. Wang, S. Z. Zu, B. H. Han, Z. X. Wei, ACS Nano., 2010, **7**, 5019-5026.
18 J. Q. Ning, T. Y. Li, J. Yan, C. G. Xu, T. Wei, Z. J. Fan, Carbon, 2013, **54**, 241-248.
19 J. W. An, J. H. Liu, Y. C. Zhou, H. F. Zhao, Y. X. Ma, M. L. Li, M. Yu, S. M. Li, J. Phys. Chem. C, 2012, **116**, 19699-19708.
20 A. E. Fischer, K. A. Pettigrew, D. R. Rolison, R. M. Stroud, J. W. Long, Nano Lett., 2007, **7**, 281-286.
21 L. Z. Fan, Y. S. Hu, J. Maier, P. Adelhelm, B. Smarsly, M. Antonietti, Adv. Funct. Mater. , 2007, **17**, 3083-3087.
22 Q. Cheng, J. Tang, J. Ma, H. Zhang, N. Shinya, L. C. Qin, J. Phys. Chem. C, 2011, **115**, 23584-23590.
23 L. L. Zhang, S. Li, J. T. Zhang, P. Z. Guo, J. T. Zheng, Chem. Mater., 2010, **22**, 1195-1202.
24 Z. Q. Niu, P. S. Luan, Q. Shao, H. B. Dong, J. Z. Li, J. Chen, D. Zhao, L. Cai, W. Y. Zhou, X. D. Chen, S. S. Xie, Energy Environ. Sci., 2012, **5**, 8726 -8733.
25 H. Jiang, P. S. Lee, C. Z. Li, Energy Environ. Sci., 2013, **6**, 41-53.
26 X. H. Cao, Z. Y. Yin, H. Zhang, Energy Environ. Sci., 2014, **7**, 1850-1865.
27 Y. X. Xu, G. Q. Shi, X. F. Duan, Acc. Chem. Res., 2015, **8**, 1666-1675.
28 C. Li, G. Q. Shi, Nanoscale, 2012, **4**, 5549-5563.
29 Y. F. Wang, X. W. Yang, L. Qiu, D. Li, Energy Environ. Sci., 2013, **6**, 477-481.
30 Y. N. Meng, K. Wang, Y. J. Zhang, Z. X. Wei, Adv. Mater., 2013, 1-6.
31 B. G. Choi, M. H. Yang, W. H. Hong, J. W. Choi, Y. S. Huh, ACS Nano, 2012, **6**, 4020-4028.
32 K. W. Chen, L. B. Chen, Y. Q. Chen, H. Bai, L. Li, J. Mater. Chem., 2012, **22**, 20968-20976.
33 M. Yu, Y. X. Ma, J. H. Liu, S. M. Li, Carbon, 2015, **87**, 98-105.
34 P. P. Yu, X. Zhao, Z. L. Huang, Y. Z. Li, Q. H. Zhang, J. Mater. Chem. A, 2014, **2**, 14413-14420.
35 S. B. Kulkarni, U. M. Patil, I. Shackery, J. S. Sohn, S. Lee, B. Park, S. C. Jun, J. Mater. Chem. A, 2014, **2**, 4989-4998.
36 L. Zhang, G. Q. Shi, J. Phys. Chem. C, 2011, **115**, 17206-17212.
37 Z.X. Tai, X.B. Yan, Q.J. Xue, J. Electrochem. Soc.,2012,**159**, A1702-A1709.
38 H. L. Wang, J. S. Tucker Robinson, X. L. Li, H. J. Dai, J. Am. Chem. Soc., 2009, **131**, 9910-9911.
39 H. P. Cong, X. C. Ren, P. Wang, S. H. Yu, Energy Environ. Sci., 2013, **6**, 1185-1191.
40 S. Liu, X. H. Liu, Z. P. Li, S. R. Yang, J. Q. Wang, New J. Chem., 2011, **54**, 369-374.
41 J. T. Zhang, J. W. Jiang, H. L. Li, X. S. Zhao, Energy Environ. Sci., 2011, **4**, 4009-4015.
42 D. W. Wang, F. Li, J. P. Zhao, W. C. Ren, Z. G. Chen, J. Tan, Z. S. Wu, L. Gentle, G. Q. Lu, H. M. Cheng, ACS Nano, 2009, **3**, 1745-1752.
43 Q. Q. Zhou, Y. G. Li, L. Huang, C. Li, G. Q. Shi, J. Mater. Chem. A, 2014, **2**, 17489-17494.
44 E. T. Kang, K. G. Neoh, K. L. Tan, Prog. Polym. Sci., 1998, **23**, 277-324.
45 M. D. Stoller, R. S. Ruoff, Energy Environ. Sci., 2010, **3**, 1294-1301.
46 H. L. Li, J. X. Wang, Q. X. Chu, Z. Wang, F. B. Zhang, S. C. Wang, J. Power Sources, 2009, **190**, 578-586.
47 Z. Mandic, M. K. Rokovic, T. Pokupcic, Electrochim. Acta, 2009, **54**, 2941-2950.
48 Q. Wu, Y. X. Xu, Z. Y. Yao, A. Liu, G. Q. Shi, Rokovic, ACS Nano., 2010, **4**, 1963-1970.
49 L. Li, A. R. O. Raji, H. L. Fei, Y. Yang, E. L. G. Samuel, J. M. Tour, ACS Appl. Mater. Interfaces, 2013, **5**, 6622-6627.
50 Q. Wang, J. Yan, Z. J. Fan, T. Wei, M. L. Zhang, X. Y. Jing, J. Power Sources, 2014, **247**, 197-203.
51 J. L. Shen, C. Y. Yang, X. W. Li, G. C. Wang, ACS Appl. Mater. Interfaces, 2013, **5**, 8467-8476.
52 C. Vall´es, P. Jim´enez, E. Muñoz, A. M. Benito, W. K. Maser, J. Phys. Chem. C, 2011, **115**, 10468–10474.

Graphical Abstract

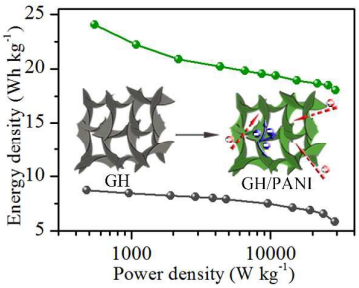

3D Graphene hydrogel (GH) provides a promising support for electrodepositing PANI, and the supercapacitor based on GH/PANI conformal heterostructure displays high energy and power densities.